Received: 20 July 2022 | Revised: 23 September 2022 | Accepted: 24 September 2022 | Published on: 13 October 2022

DOI: 10.1002/mrm.29490

RESEARCH ARTICLE

Magnetic Resonance in Medicine

Scalable and modular 8-channel transmit and 8-channel flexible receive coil array for ^{19}F MRI of large animals

Ali Caglar Özen[1] | Felix Spreter[1] | Waldemar Schimpf[1] | Johannes Fischer[1] | Serhat Ilbey[1] | Simon Reiss[1] | Alexander Maier[2] | Dominik von Elverfeldt[1] | Timo Heidt[2] | Constantin von zur Mühlen[2] | Michael Bock[1]

[1]Department of Radiology, Medical Physics, Medical Center–University of Freiburg, University of Freiburg, Freiburg, Germany

[2]Department of Cardiology and Angiology I, University Heart Center, Medical Center–University of Freiburg, University of Freiburg, Freiburg, Germany

Correspondence
Department of Radiology, Medical Physics, Medical Center–University of Freiburg, University of Freiburg, Freiburg, Germany.
Email: ali.oezen@uniklinik-freiburg.de

Funding information
Deutsche Forschungsgemeinschaft, Grant/Award Numbers: BO 3025/17-1, MA 7059/3-1, SFB1425#422681845

Purpose: To introduce an RF coil system consisting of an 8-channel transmit (Tx) and 8-channel receive (Rx) coil arrays for ^{19}F MRI of large animals.

Methods: The Tx efficiency and homogeneity of the 8-element loop coil array (loop size: 6×15 cm^2) were simulated for two different pig models rendered from MR images. An 8-channel Rx coil array consisting of a flexible 6-channel posterior and a 2-channel planar anterior array was designed to fit on the abdomen of an average-sized pig in supine position. Measurements were performed in a grid phantom and ex vivo on a pig model with perfluoroctylbromide (PFOB)–filled tubes inserted in the thorax.

Results: Measured and simulated Tx efficiency and homogeneity for the 8-channel and 5-channel arrays were in good agreement: $1.87 \pm 0.22\mu T/\sqrt{kW}$ versus $1.96 \pm 0.29\mu T/\sqrt{kW}$, and $2.29 \pm 0.39\mu T/\sqrt{kW}$ versus $2.41 \pm 0.37\mu T/\sqrt{kW}$. An isolation of 38 ± 8 dB is achieved between the ^{19}F Tx and Rx elements, and over 30 dB between the ^{1}H and ^{19}F elements. The PFOB-filled vials could be clearly identified within the cadaver abdomen with an SNR of 275 ± 51 for a 3D gradient-echo sequence with 2-mm isotropic resolution and 12 averages, acquired in 9:52 min:s. Performance of the Tx array was robust against phase and amplitude mismatches at the input ports.

Conclusions: A modular and scalable Tx array offers improved Tx efficiency in ^{19}F MRI of large animals with various sizes. Although conventional birdcage coils have superior Tx efficiency within the target region of interest, scalability of the Tx array to animal size is a major benefit. The described ^{19}F coil provides homogeneous excitation and high sensitivity detection in large pig models.

1 | INTRODUCTION

^{19}F MRI has been implemented successfully in rodents to study myeloid cell uptake and migration after myocardial infarction (MI) and in atherosclerosis,[1–6] but only few reports are published in which this imaging method has been used in human-size models such as pigs[4,6]; however, the transfer of ^{19}F MRI into large animals is crucial for both method validation and development of clinical applications. A major challenge of upscaling the ^{19}F MRI studies to larger animals is the design and construction of a dedicated ^{19}F RF coil system. At B_0 = 3 T, the Larmor frequency of the ^{19}F nucleus of 120.2 MHz is only 7.5 MHz lower than that of ^{1}H with 127.7 MHz, which requires special decoupling circuits to avoid unwanted coupling. Furthermore, electromagnetic and mechanical compatibility with the existing ^{1}H RF coils is also required for studies in which interleaved measurements of multiple nuclei are performed. Another limitation is the low peak RF power of the broadband transmit system for X-nuclear MRI: In clinical 3T whole-body MRI systems, often RF power amplifiers with only a few kW are available at the ^{19}F frequency, whereas the narrow-band transmitter for conventional ^{1}H MRI can deliver peak powers up to 15 kW and more. In general, target design parameters for a ^{19}F coil system are homogeneous excitation and high SNR within the target anatomy (in this case, the heart). Unlike ^{1}H MRI, in ^{19}F MRI, the signal solely originates from the administered ^{19}F tracers, and no background signal from the body is present. Thus, the effective imaging volume can be restricted to a specific tissue or organ.

Various multinuclear coils have been designed for preclinical studies on small animals.[7] A double-tuned birdcage coil can be realized using either a trap circuit[8,9] or a PIN diode,[10] and mechanical actuators were proposed to avoid losses from the PIN diode.[11] To construct multinuclear birdcage coils, alternating rungs were individually tuned to two different frequencies,[12,13] or the end rings were designed as four-ring birdcage coils.[14] However, double-tuned birdcage coils are difficult to realize when the two resonance frequencies are very close. In Joseph et al, two degenerate modes were tuned to the ^{19}F and ^{1}H resonances by nonuniform distribution of capacitances in the rungs of birdcage coil.[15] Insertion of an additional shield with a smaller diameter was also proposed to switch the resonance frequency to ^{19}F Larmor frequency.[16] Muftuler et al suggested an automatically tuned birdcage coil using variable capacitance (varactor) diodes.[17] A double-tuned birdcage coil was developed using the coupled resonator method.[18] In Choi et al,[19] PIN diodes with inductors were used to dual-tune a birdcage to the ^{19}F and ^{1}H frequencies.

A double-tuned coil can also be constructed using separate coils, such as two birdcage coils in co-axial configuration[20–23] or concentric loops.[24,25] Although each coil resonates at a different frequency, mutual coupling can cause interference between the coils due to induced current between the loops. Counter-rotating currents can cause significant loss in magnetic field intensity of the coils.[21] Geometric decoupling can also be used in double-tuned coils.[26–30] Although there are many examples of ^{19}F coils for small animal measurements, only a few designs were demonstrated for human and large animal applications: ^{19}F knee MRI at 7 T,[31] human liver MRS,[32] and lung MRI[33] at 1.5 T, pig at 3 T using a dual-tuned transmit (Tx), and a ^{19}F-surface loop coil.[34] In general, dual-tuned ^{19}F/^{1}H coils show an inferior performance compared with mononuclear coil designs.[7,18] In clinical studies, use of the conventional ^{1}H coils for ^{1}H MRI increases reproducibility and intersubject consistency. Therefore, in this study, we use mononuclear RF coil systems for ^{19}F MRI. The advantages of using mononuclear coils that are easily exchangeable to allow consecutive measurements on the same animal have also been demonstrated for preclinical setups at different field strengths.[35,36] As a design target, we also ensured that ^{1}H and ^{19}F coils can easily be exchanged without moving the animal.

The purpose of this study is to introduce an RF coil system for ^{19}F cardiac MRI at 3 T in a pig model. We developed an 8-channel Tx and 8-channel receive (Rx) coil array tuned to 115.9 MHz that can be used in combination with existing commercial ^{1}H RF coils. The coils were designed to have high transmit efficiency with homogeneous field distribution, and high sensitivity within the target volume of the heart. For Tx coil design optimization, finite-difference time-domain (FDTD) simulations were performed to compare 8-channel independent loop elements to a high-pass birdcage coil for different animal sizes. To improve Tx efficiency, a coil housing was constructed that can be adapted to animals of various sizes. An Rx coil array was designed to fit tightly on the curved abdomen of a large pig. The performance the ^{19}F RF coil system was evaluated in silico, in phantom, and ex vivo.

2 | METHODS

In the following, the design of the ^{19}F RF coil system is described, which consists of an 8-element Tx volume coil array, and an 8-element Rx surface coil set distributed to anterior and posterior parts. All coil elements were designed as single-resonant systems operating at the ^{19}F frequency, and for the ^{1}H MRI measurements, a surface coil array with 18 loop elements arranged in

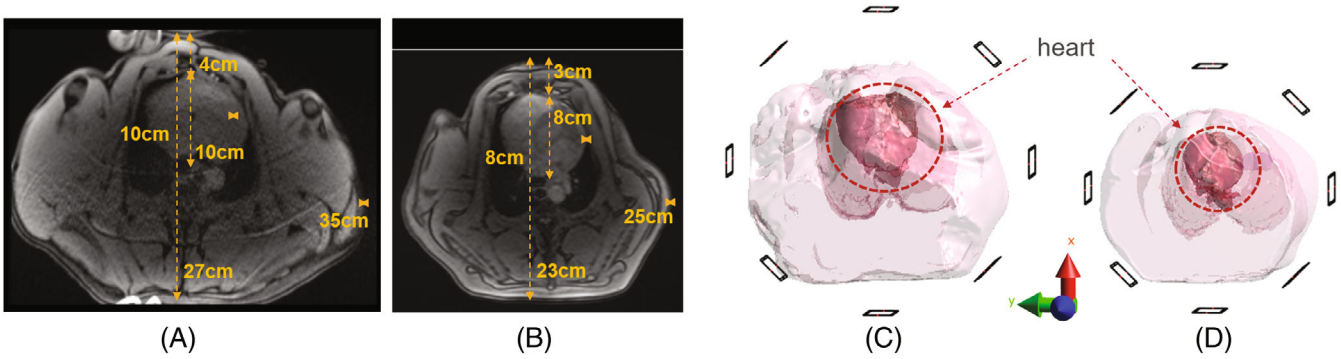

FIGURE 1 The animal size may differ significantly. Simulation settings to test the effect of the size of the volume covered by the transmit (Tx) array are driven by real animal models. A transverse slice from the 3D-FLASH image of a large (A) and small pig (B). The Tx array element models covers a larger volume to enclose the large pig model, where, the heart is indicated with a darker color and around the heart, lungs are visible (C). Large pig large coil (LPLC) model (C). Small pig and small coil (SPSC) model (D). The distance between the neighboring coils in LPLC and SPSC configurations is measured as 104.6 mm and 89.3 mm, respectively

3 × 6 matrix form (Body 18; Siemens Healthcare) was used. To determine the optimal geometry of the RF coil system, T_2-weighted 3D-FLASH ^{1}H images (voxel size: $2 \times 2 \times 3\,mm^3$) of previous animal experiments were segmented using 3D Slicer,[37] in which the pig is in a supine position on the patient table. In transverse images, the heart was very close to the anterior chest surface, and it extended from 4 to 13 cm into the thorax for the large animal and 3 to 11 cm for the small animal (Figure 1A,B). For two different animal sizes (small and large pig), the heart, the lung, and the outer contour of the animals were manually segmented (Figure 1C,D). Based on these geometric data, the following Tx coil array and tight-fitting Rx coil array designs were realized.

2.1 | Transmit array

Based on the geometries of the thorax, an outer Tx coil array was designed for RF excitation that consists of eight independent loop coils (size: $6 \times 15\,cm^2$; Figure 2D) symmetrically arranged in a circle (Ø = 42 cm) around the animal and the Rx coils, five of which are fixed on a detachable upper section made of a polycarbonate (Figure 2C). The Tx loop coil elements were etched on a 1.6-mm-thick FR4 printed circuit board with a 105-µm-thick Cu layer (Figure 2D). Each loop was segmented by four symmetrically distributed tuning capacitors, and it was matched to 50 Ω by series capacitors (25-8R2-G-2500-S; Voltronics). Variable capacitors (60-0752-15 005-901; Alfred Tronser) were added in parallel to the tuning capacitor at the feed port and the matching capacitors. Active detuning was implemented using a high-power PIN diode (MA4PK2000; MACOM). The coil elements were attached to the cylindrical coil former by 3D-printed (i3 Mk3S; Prusa Research) spacers (Figure 2C). The spacers allowed modularity and scalability of the Tx array. For tight fitting of the coils also to the smaller animals, spacers allowed to adapt the inner diameter of the Tx array so that the Tx elements are always close to the thorax. The spacers were designed as detachable mounts that hold the Tx coil elements and can be slid and fixed to the rails on the coil holder. If the coil elements are mounted on 12-mm or 72-mm spacers, the inner diameter of the Tx array is scaled from 420 mm to 300 mm, respectively. Spacers also allowed modularity by simply removing the coil elements and configuring arrays with fewer channels using the same coil holder.

The Tx coil was connected to a clinical 3T MRI system (Prisma Fit; Siemens Healthcare), which was equipped with a broadband RF power amplifier (8 kW peak power, 30–130 MHz, LPPA 13080 W; Stolberg HF-Technik) that can provide 3.2 kW peak RF power at 115.9 MHz with a maximum pulse duration of 3 ms. To split the RF power equally to each channel, an eight-way and a five-way high-power Wilkinson power dividers were designed so that the Tx coil could either be used with all eight channels, or with only the anterior five channels for cardiac applications (Figure 2E). To drive the eight-channel/five-channel Tx coil in circularly polarized mode, 45°/72° phase increments between the adjacent channels were introduced by adjusting the length of the coaxial cables between the coil elements and the output ports of the power divider. A schematic diagram of the interface between the Tx coils and the MRI system is shown in Supporting Information Figure S1. *S*-parameters S_{ij}, B_1^+ homogeneity, and transmit efficiency of the Tx coil were measured. Printed circuit board layouts for the coil elements and the power divider are available at https://github.com/ozenEEE/UKF_19FCOIL.

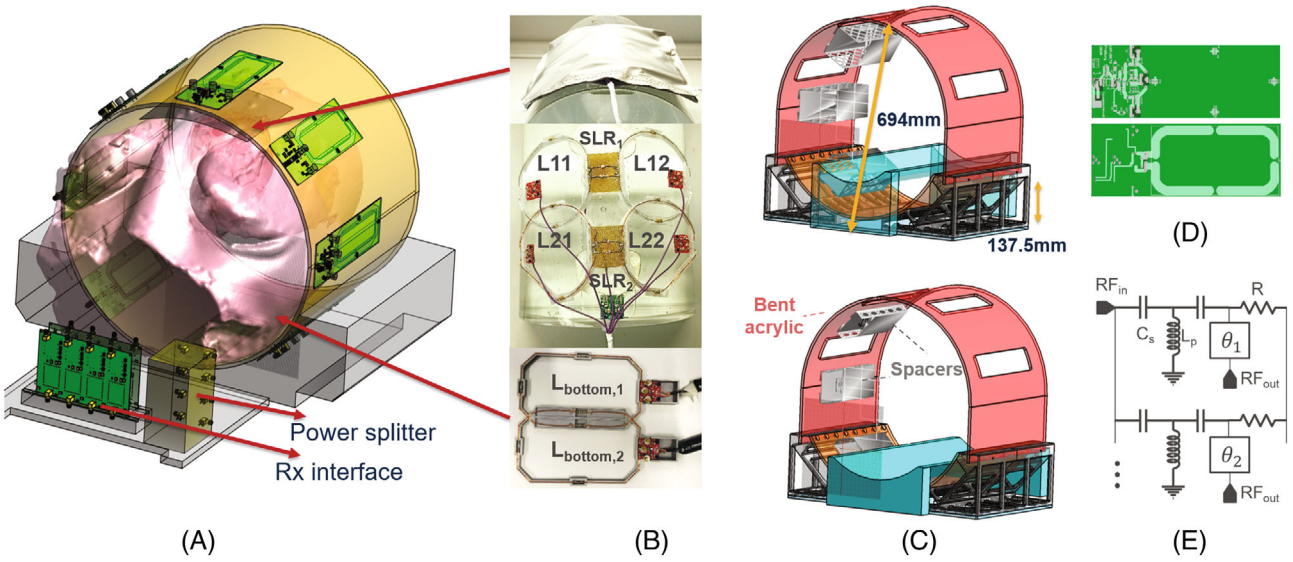

FIGURE 2 Schematic and layout of the dedicated ^{19}F-MRI RF coil system. Complete system model visualized with the coils and the interface circuit positions (A). Photos of the anterior and posterior receive (Rx) coil elements (B). Anterior Rx elements (ie, L11, L12, L21, L22, and shielded loop resonators [SLRs])[1,2] are covered by a medical-grade synthetic leather housing (top). The 3D model of the main coil holder (C). Spacers to scale the coil arrangement from large to small are demonstrated in the bottom and top rows, respectively. Layouts of the top and bottom layers of the printed circuit boards used to construct the Tx coil elements (D). Schematic of the n-way Wilkinson power divider (E).

2.2 | Receive array

An inner Rx coil array with eight channels was constructed that consists of a six-channel semiflexible anterior and a two-channel rigid planar posterior array (Figure 2B). Four of the anterior elements and the two posterior elements were constructed from enameled copper wire (Ø: 1 mm) that were fixed in 3D-printed polyethylene terephthalate glycol-modified wire tracks. The elements were segmented by two tuning capacitors and series-matching capacitors (S111DUE; Johanson Technology), and variable capacitors (JR300 [Knowles Voltronics] or BFC280811339 [Vishay Electronic]) were added in parallel to the tuning capacitor at the feed port and the matching capacitors. The other two anterior Rx coil elements were shielded loop resonators (SLRs)[38–42] driven in self-resonance,[42] which were constructed using a 22-cm-long semirigid coaxial cable (SUCOFORM_47_CU; Huber+Suhner) with a single gap on the shield symmetric to the feed port. Active detuning was implemented using a PIN diode (MA4P7102F-1072T; MACOM) in parallel to the tuning capacitor at the feed port. Preamplifier decoupling was achieved by adjusting the length of the coaxial cable (G_02232_D; Huber+Suhner) between the Rx coil and the preamplifier (Stark Contrast). Detailed circuit schematics and component values can be found in https://github.com/ozenEEE/UKF_19FCOIL. A schematic diagram of the interface between the Rx coils and the MRI system is shown in Supporting Information Figure S2.

The anterior loop coil elements were arranged as a 2×2 matrix, in which the two elements in the first row were realized as loops with a diameter of 12 cm, and the loop elements in the second row were shaped to fit between the legs of a pig (see Figure 2B). Two SLR elements were placed between the loop coil elements (Figure 2B). The neighboring loop coil elements in a column were decoupled by geometrical overlapping, whereas the elements in each row were decoupled capacitively. This decoupling strategy has two advantages: First, a better isolation is achieved as the next nearest neighbors are further away from each other (Supporting Information Figure S3). Second, capacitive decoupling is less sensitive to small changes in coil geometry, which allows us to bend the anterior coils around the animal's dome-shaped thorax to maximize the filling factor. The rigid posterior part consists of two geometrically decoupled rectangular coils of 8×14 cm size, which are fixed below a platform that is used for animal positioning (Figure 2B).

Performance of the Rx coil array was characterized in the test bench using a network analyzer (ZVB4; Rohde & Schwarz) to measure the S-parameters, S_{ii}, and in the MRI system to determine the ratio of loaded and unloaded quality factors, $Q^i{}_L/Q^i{}_{UL}$, both in a phantom and in vivo without changing the tuning and matching. For this, a tissue-mimicking phantom was prepared using 13.6 L distilled water with 3 g/L NaCl and 1 g/L $CuSO_4$ filled in a half-cylinder container (Ø: 20 cm, height = 40 cm). Phantom liquid had $\varepsilon_r = 78.2$ and $\sigma = 0.46$ S/m at

115.9 MHz measured with DAKS12 (Zurich Med Tech). The *S*-parameters were also measured in vivo inside the MRI system.

2.3 | Simulations

To assess the effect of animal size, coil arrangement (tight vs distant placement with respect to the body) as well as amplitude, phase mismatches, and electromagnetic field simulations were performed on the Tx array elements using the FDTD solver of Sim4Life (v6.2; Zurich Med Tech). Simulation results were used to calculate the B_1^+ homogeneity, Tx efficiency, and the maximum 10 *g*–averaged peak local specific absorption rate (SAR_{10g}). Again, the two different animal models, a large pig (LP) and a small pig (SP), were used as shown in Figure 1C,D. The lungs and the heart were modeled as separate uniform organs with isotropic dielectric properties of lung parenchyma and heart muscle, respectively,[43] and the rest of the body was assigned $\varepsilon_r = 78$ and $\sigma = 0.5$ S/m. Coil conductors were modeled as perfect electric conductors. For the simulation, the coils were first tuned to 115.9 MHz with a series of multiport broadband simulations with a 100-MHz bandwidth. Once a reflection coefficient ≤ 15 dB was achieved for all of the coil elements, a harmonic simulation was performed. The Tx arrays were driven in CP mode under ideal matching conditions with the real parts of the input impedances equal to the source impedance. For comparison, an eight-leg high-pass birdcage coil of the same diameter was modeled and simulated. To demonstrate the scalability of the Tx array, a tight-fit Tx array for the smaller pig model was simulated in which spacers were introduced to bring the Tx array elements closer to the animal. In the simulations, B_1^+ homogeneity, Tx efficiency, and SAR_{10g} were evaluated in the following nine scenarios:

1. Large pig model and large-diameter Tx array (LPLC);
2. Birdcage coil with the same diameter as the LPLC case, yet longer in z direction (rung length = 40 cm), evaluated with small and large pig models (LPBC and SPBC);
3. Small pig model large-diameter Tx array (SPLC);
4. Small pig model and tight-fit Tx array with spacers (SPSC); and
5. Both pig models, upper five and seven elements of the Tx array configurations (LPLC7x, LPLC5x, SPSC7x, and SPSC5x).

B_1^+ homogeneity was evaluated across the heart. As a figure of merit, peak deviation from the mean value within the heart was calculated. To test the effect of imperfections in the power splitting, differences in phase shifters, as well as reflections, B_1^+ homogeneity was evaluated for various combinations of the Tx array elements with random amplitude and phase deviations within 20% of the CP-mode values (ie, equal amplitude and 360/*N* phase increment, where $N = 5$ or 8 is the number of Tx channels). Transmit efficiency was calculated as $|B_1^+|/\sqrt{P_{in}}$ in $\mu T/\sqrt{kW}$. All of the results were normalized to total input power of 3 kW (details of the simulation settings are provided in the Supporting Information. Pig models and the Python scripts used in analysis of the simulation results can be downloaded from https://github.com/ozenEEE/UKF_19FCOIL.

To test the scalability of the Tx coil system to higher field strengths, the individual coil elements were tuned to 19F Larmor frequencies at 7 T, 9.4 T, and 10.5 T at 280, 376, 420 MHz, respectively. Field simulations were performed for the SPSC case, and CP-mode results were compared with the 3T (116 MHz) results. Excessive B_1^+ inhomogeneity is expected at ultrahigh fields already starting from 4 T.[44,45] To achieve a homogenous excitation at beyond 4 T, B_1 shimming is required.[46–50] To show that B_1 shimming can improve the homogeneity, an optimization algorithm was run with the phase values of the individual coils being the free parameters, and $\log\left(\max\left\|B_1^+\right\| / \min\left\|B_1^+\right\|\right)$ the objective function calculated within a volume that covers the whole heart. The integrated optimization package of Sim4Life v7.0 was set up for a global search method based on Jones et al,[51] with maximum number of iterations limited to 300. The optimization routine started with the initial eight optimization variables with a 45° phase shift. The RF shimming results for the optimal solution were incorporated in the postprocessing step, and the objective function was compared with the CP-mode results.

2.4 | Magnetic resonance imaging measurements

A ^{19}F grid phantom filled with perfluoropolyether lubricant (Fomblin Y LVAC 16/6; Solvay Fluor) was prepared to assess the coil performance. The phantom consists of acrylic tubes (ø = 10 mm) that are distributed over a homogeneous 1 g/L $CuSO_{4(aq)}$ body ($300 \times 200 \times 400\ mm^3$) as shown in Figure 3I. The SNR analysis was performed using a 3D gradient-echo sequence with TR/TE = 8.4/4 ms, α = 30°, 2-mm isotropic resolution, FOV = $240 \times 320\ mm^2$, 120×160 acquisition matrix, 120 slices, 12 averages, and 09:52 min:s total acquisition time. A 3-ms-long Gaussian RF pulse was programmed to excite only the central line of the perfluoropolyether spectrum so that chemical shift artifacts caused by the multiple ^{19}F-resonances are avoided. B_1^+ maps were calculated using the double-angle method[52]

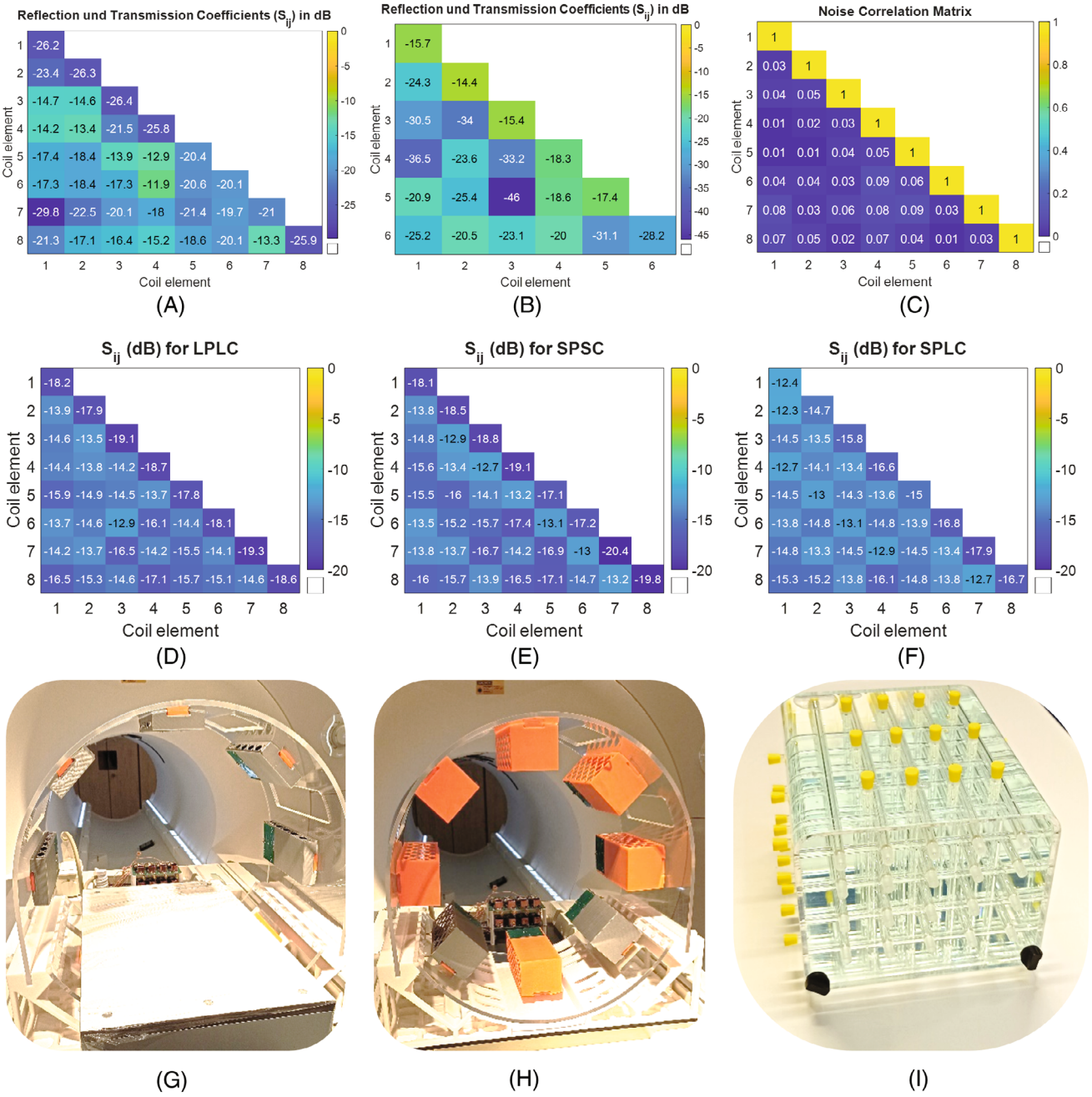

FIGURE 3 Reflection, coupling, and noise correlation matrices. The S matrix of the Rx array measured with phantom (A) and in vivo (B) loading. In the phantom, an Sii < −20 dB and an Sij < −12 dB were achieved, and in the animal an Sii < −14 dB and an Sij < −19 dB were achieved. Noise correlation matrix of the Rx array (C). Reflection and transmission coefficients of the Tx array elements for large phantom and large coil (D), small phantom and small coil (E), and small phantom and large coil (F). Photos of the large (G) and the small (H) coil, respectively. Photo of the large-grid phantom (I). The coils were tuned initially for the large-phantom and large-coil setting. No additional tuning and matching were applied

using the same acquisition matrix for $\alpha_1/\alpha_2 = 20°/40°$. To demonstrate modularity, the same measurements were also repeated using the upper five elements of the ^{19}F Tx array. A five-channel Wilkinson power splitter was also interfaced to the Tx output of the MRI system. Receive coil noise correlation matrix was computed from a noise-only scan. The ^{1}H MR images were acquired using the same imaging parameters as in the ^{19}F protocol, but with a single average and $1 \times 1 \times 2\,\text{mm}^3$ voxel size using the system's body matrix coil. For ^{1}H MRI, the ^{19}F coils were unplugged, the anterior ^{19}F Rx array and the upper part of the Tx array (ie, five elements) were removed, and the remaining coil elements were manually detuned by a battery-supplied detuning signal (Supporting

Information Figure S4). To test the coil system under realistic conditions, a cadaver measurement was performed on a pig using a 3D-printed heart-shaped phantom with six perfluorooctylbromide (PFOB)–filled acrylic tubes that was introduced into the thorax after the heart was removed. During the measurements, because the phantoms and the cadaver were not moved for the ^{19}F and ^{1}H coil exchange, the data sets were intrinsically co-registered. For imaging, the same imaging protocol was used as the grid-phantom measurements. To demonstrate scalability, MRI of the heart phantom with PFOB tubes was acquired with the 12-mm and 72-mm spacers corresponding to LC5x and SC5x arrangements, respectively.

Finally, to test the detection sensitivity, we mixed two different PFCs, PFOB and FC-84 (perfluoroheptane, Fluorinert; 3 M), because PFOB is not soluble in water and only minimally soluble in oil (37 mM/L). The CF_2Br peak of the PFOB is separated by 1.97 kHz from the closest peak of the FC-84.[53] The 5-ml Eppendorf tubes with PFOB/FC-84 volume ratio of 0.1, 0.25, 0.5, 0.75, and 1 (pure PFOB) were prepared. Exciting only the CF_2Br frequency with a narrow-band pulse using the LC setup and the same receive arrays, the SNR of each tube was calculated[54] for the same imaging protocol as the phantom and cadaver tests.

3 | RESULTS

In vitro and in vivo S_{ij} matrices are shown in Figure 3. The S-matrix of the Tx array shows that the isolation between the elements is higher than 13 dB, and the input impedance of each coil is close to 50 Ω (Figure 3A–C). The Wilkinson power divider introduced an additional insertion loss up to 1.5 dB at the output ports. The amplitude deviation from the ideal value was measured to be < 12% for both five-way and eight-way power dividers. Incremental phase for the CP mode deviated by $< \pm 3.5°$, and $\pm 6.1°$ for eight-way and five-way power divider, respectively. When the Tx coils are used with spacers (small pig arrangement; Figure 3B), reflection coefficients improve by up to 5.7 dB compared with the larger coil diameter (Figure 3C) due to higher loading.

For the Rx array, coupling between the elements was always below −16 dB without preamplifier decoupling, which improves the isolation by up to 18 dB. An isolation of 38 ± 8 dB was measured between the ^{19}F Tx and Rx elements. Between the phantom and in vivo, S parameters deviate < 10%, which demonstrates that the RF coil is not sensitive to load variations. The ratio, $Q^i{}_L/Q^i{}_{UL}$, was below 0.45 for all RF coil elements, which indicates that the sample noise is dominant for the Rx array, whereas for the Tx array most of the RF energy is absorbed by the load.

In Figure 4, simulated $B_1{}^+$ maps for various pig and coil pairs are shown for a transverse slice across the center of the heart. Using seven-channel and five-channel coils increases Tx efficiency in the heart compared with eight channels for the same total input power. Scalability was demonstrated in simulations in which the coil elements were placed to form an array of a smaller diameter of 300 mm, and 40.2% higher Tx efficiency was computed for SPSC compared with the SPLC case.

Quadrature birdcage coils have a higher Tx efficiency for both small and large pigs. Compared with the SPBC and LPBC settings, SPSC5x and LPLC5X has up to 35% and 62% lower Tx efficiency, respectively. The $B_1{}^+$ line profile analysis showed that the Tx homogeneity is better than 30% for all cases except for LPLC, in which up to 45% deviation from the mean is observed along the line profile, L1 (ie, the head–foot direction) (Supporting Information Figure S5). Field combinations with 20% random deviations from CP resulted in < 6% deviation in $B_1{}^+$ homogeneity (Supporting Information Figure S6). For the smaller pig, birdcage and the smaller coil array have superior homogeneity in the longitudinal direction.

An axial slice from the $B_1{}^+$ simulations for the eight-channel Tx array tuned for 7 T, 9.4 T, and 10.5 T are shown in Figure 4. At the ultrahigh frequency band (ie, 0.3–1.0 GHz), CP mode yields extremely inhomogeneous $B_1{}^+$ with deviations up to 80 dB between the minimum and maximum $B_1{}^+$ magnitude, even for a limited volume of interest (Figure 5E). After phase-only RF shimming, the objective function (ie, $\log\left(\max\left\|B_1^+\right\| / \min\left\|B_1^+\right\|\right)$) is improved by 44, 30, and 27 dB at 7 T, 9.4 T, and 10.5 T, respectively. The resulting phases assigned to each channel were $\emptyset_{7T} = \{118,120,181,282,294,60,220,152\}°$, $\emptyset_{9.4T} = \{127,4,313,359,224,20,121,1\}°$, and $\emptyset_{10.5T} = \{340,2,81,224,359,1,176,38\}°$. For the 9.4T and 10.5T simulations, the optimization algorithm did *not* converge; however, the phase values for the best objective among the tested cases was assigned.

In Table 1, peak local SAR values at 3-kW input power are given for all pig sizes and coil pairs. As expected, when the coil elements are further away from the body in the SPLC case, the peak SAR_{10g} decreases. In the SPSC arrangements, the distance between the coil elements and the body is slightly larger than the LPLC case (~5 mm). Thus, consistently lower peak SAR10g was calculated for SPSC than for LPLC. For lower number of Tx array elements, the peak SAR_{10g} is also higher as the peak RF power per coil increases, with the exception of SPSC5x, which has the lowest peak SAR_{10g}.

The measured Tx efficiency/homogeneity values were comparable with the simulation results: For the eight-channel Tx coil, Tx efficiency was calculated as $1.87 \pm 0.22\ \mu T/\sqrt{kW}$ versus $1.96 \pm 0.29\ \mu T/\sqrt{kW}$ from the

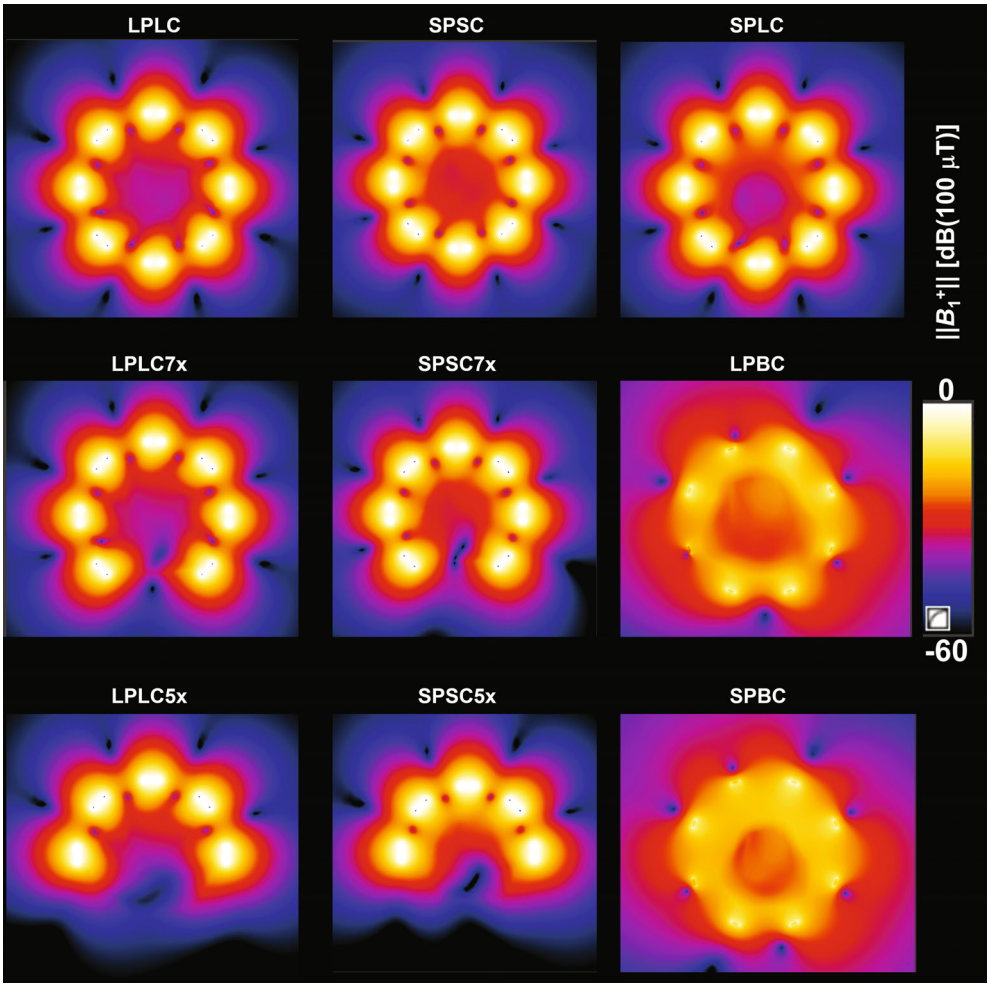

FIGURE 4 Normalized $||\boldsymbol{B}_1{}^+||$ maps for a transverse slice across the center of the heart are shown for LPLC with eight (LPLC), seven (LPLC7x), and five (LPLC5x) channels; SPSC with eight (SPSC), seven (SPSC7x), and five (SPSC5x) channels; small pig and large coil (SPLC), large pig and birdcage coil (LPBC), and small pig and birdcage coil (SPBC). Birdcage coils are driven in quadrature mode. All of the field maps are generated for 3 kW total input power distributed equally among the Tx coil input ports

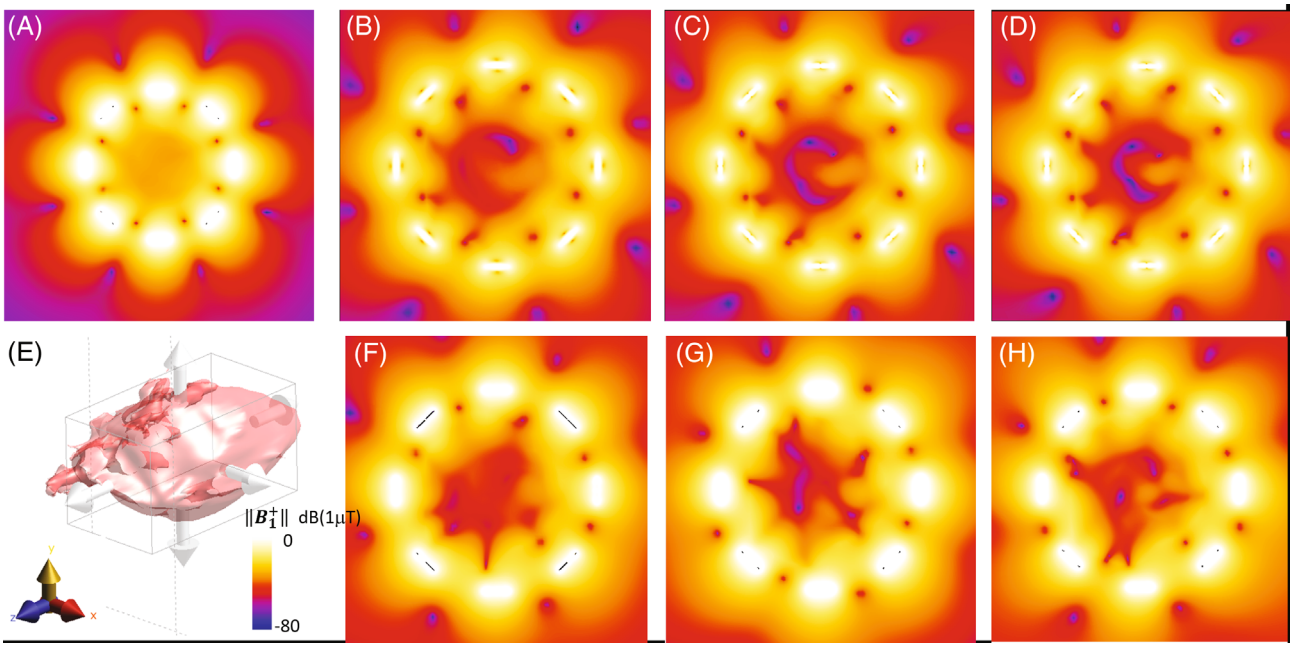

FIGURE 5 The $||\boldsymbol{B}_1{}^+||$ maps for a transverse slice across the center of the heart are shown for the SPSC case with the coil elements tuned at 3 T (A), 7 T (B), 9.4 T (C), and 10.5 T (D) Larmor frequencies for ^{19}F, corresponding to 116, 280, 376, and 420 MHz, respectively. CP mode yields homogeneous field distributions at 3 T. However, at ultrahigh fields, deviations up to 80 dB are observed. The B_1 shimming improved the homogeneity in the selected volume (E) by 44, 20, and 24 dB for 7 T (F), 9.4 T (G), and 10.5 T (H), respectively.

TABLE 1 Peak local 10 g–averaged specific absorption rate values for the given pig size and coil combinations, normalized to 3 kW for the Tx array, to 1020 W for the birdcage simulations

Coil	LPLC8x	SPSC8x	SPLC8x	LPLC7x	SPSC7x	LPLC5x	SPSC5x	LPBcage	SPBcage
Peak SAR_{10g} (W/kg)	137	87	82	156	118	222	63	200	140
Max deviation (%)	6	5	4	8	7	9	10	NA	NA

Abbreviations: NA, not available; SAR_{10g}, peak local 10 g–averaged specific absorption rate.

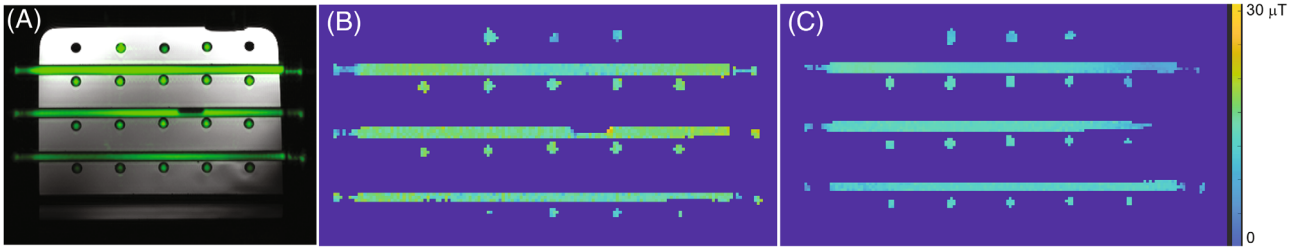

FIGURE 6 ^{19}F MRI of the grid phantom acquired with the LPLC arrangement, overlaid on the ^{1}H image acquired with the body matrix (A). The B_1^+ maps for the five-channel (B) and eight-channel (C) Tx array (LC arrangement) driven in CP mode.

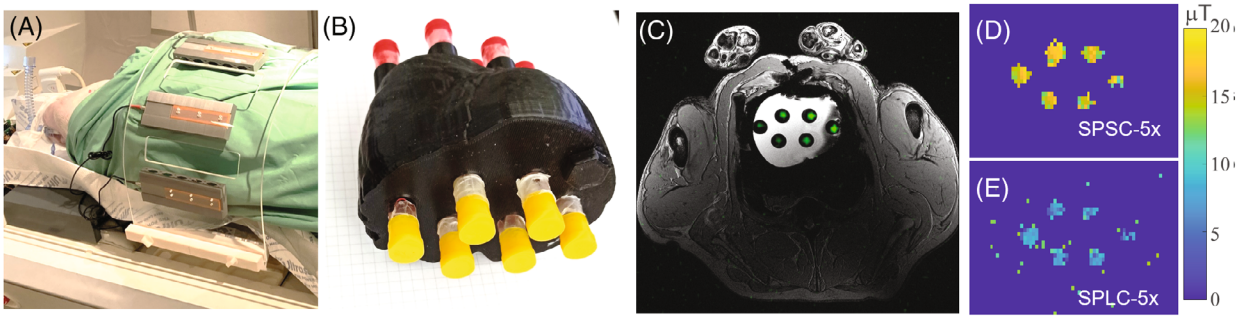

FIGURE 7 Ex vivo ^{19}F MRI using the eight-channel Tx and eight-channel Rx coil system. Photo of the cadaver measurement setup (A). The 3D-printed phantom rendered from high-resolution heart images of a large pig with six perfluoroctylbromide-filled tubes (B). Transverse slices of the cadaver, in which the ^{19}F image (green) is overlaid on the ^{1}H gradient-echo (gray) image (C). The B_1^+ maps for SPSC5x (D) and SPLC5x (E) configurations are shown to verify simulation results that demonstrate scalability

measured and simulated B_1^+ maps, respectively. When only the upper five elements were used (ie, LPLC5x), Tx efficiency was 2.29 ± 0.39 $\mu T/\sqrt{kW}$ versus 2.41 ± 0.37 $\mu T/\sqrt{kW}$ in the measured and simulated B_1^+ maps, respectively. The higher Tx efficiency for the lower number of channels is also visible in the axial slices from the measured B_1^+ maps given in Figure 6B,C. For SPSC, SPSC7x, and SPSC5x cases, Tx efficiency increased from 2.91 ± 0.34 $\mu T/\sqrt{kW}$ to 3.55 ± 0.57 $\mu T/\sqrt{kW}$ and 4.48 ± 0.81 $\mu T/\sqrt{kW}$, respectively. Only eight-channel and five-channel large coil arrangements were tested experimentally due to the grid-phantom size. Note the reduced sensitivity in the central tube in the top row, which can be attributed to the lower Rx coil sensitivity along the center of the anterior coil array (Figure 6). Scalability was also demonstrated using the heart-shaped PFOB phantom (Figure 7D,E), in which the phantom size corresponds to a small pig and the SPSC5x and SPLC5x configurations were compared. A similar result as the simulations, comparing the SPSC5x and SPLC5x cases, was also obtained by phantom MRI measurements. Here, the SC5x case yielded 31.3% higher transmit efficiency than LC5x for the PFOB heart phantom (Figure 7D,E). No coupling between the 19F Tx coils and the integrated ^{1}H body coil was observed.

For the ^{1}H imaging, only the upper five elements of the Tx array and the flexible Rx array placed on the top could be removed. A decoupling over 30 dB between the ^{1}H and the remaining ^{19}F elements was measured. To determine the reproducibility of the ^{19}F signal, 10 acquisitions were then performed using the transmitter voltage of 64 V. For this reference transmitter voltage, a mean SNR of 79 ± 3 was observed for the ^{19}F signal from the perfluoropolyether liquid at the central transverse slice.

This translates into a signal variation of 3.8%, assuming the noise is constant.

The PFOB-filled vials could be clearly identified inside the cadaver with an SNR of 275 ± 51 for a 3D gradient-echo sequence with 2-mm isotropic resolution and 12 averages, acquired in 9:52 min:s. The overlay of ^{19}F images (green) and ^{1}H anatomical images (gray) provides visualization of the PFOB at the area of myocardium (Figure 7).

In the sensitivity tests, the image SNR was < 10 for 10% and 25% PFOB solutions (Supporting Information Figure S7). Detection sensitivity is calculated as 2193/mol in image SNR. Note that this measurement accounts only for the CF_2Br peak.

4 | DISCUSSION

In this study, an eight-channel Tx/eight-channel Rx RF coil array was developed for ^{19}F MRI of large animals at 3 T. The coil setup can be used in combination with clinical ^{1}H coils by allowing removal of the ^{19}F coils during ^{1}H imaging without moving the animal. The RF coil array was tested in a grid phantom and an ex vivo pig model under various loading conditions. A modular and scalable design scheme was introduced using spacers to adapt the Tx coils to various animal sizes. The proposed 19F coil system differs from other coil designs in that it combines the use of spacers for the Tx coil elements to be able to adapt the circumference of the Tx array with a modular design, where the number of Tx elements can be changed, and a receive coil system with different decoupling techniques (capacitive and geometric) having a hybrid design made of loops and SLRs.

The proposed coil system can be used, for example, to investigate MI. Myocardial infarction is one of the main causes of mortality and long-term disability worldwide.[55] After MI, the imbalance of the monocytes' inflammatory and reparative response leads to aggravated myocardial damage and suboptimal tissue repair. Currently, novel therapeutic strategies are being investigated that modulate monocyte migration and response to MI, to limit ischemic damage and to promote healing. Thus, there is an urgent clinical need to develop and validate new in vivo readouts of monocyte migration and response after MI as a potential prognostic marker of cardiac outcomes, or to characterize the efficacy of new immune-modulating compounds. The proposed coil can also be used to track rapid myeloid cell egress from the spleen and bone marrow.[56]

The results show that the Tx array driven in CP mode provides a homogeneous excitation field over the heart region with < 15% deviation from the mean. The modular design enabled us to use five channels as well to increase the RF power per channel, thereby improving the transmit efficiency while keeping the B_1^+ homogeneity within 19% of the mean. Decreasing the size of the coil by replacing the thin by thicker spacers allowed us to scale the coil to the animal size. The results showed that 31.3% higher B_1^+ can be obtained when Tx coil array is arranged to form a cylinder with a smaller diameter.

As seen in the FDTD simulations, a homogeneous B_1^+ distribution can be created over the heart of an adult pig with an array of local Tx loop coils. In combination with an Rx coil array, also a high SNR can be achieved if the Rx coil shape conforms to the anatomy of a pig in supine position. More detailed modeling of pig anatomy and coils could also increase the accuracy. In Carluccio et al,[57] it was reported that anatomical modeling with fewer tissue segments does not result in significant changes in local SAR; therefore, it might be preferred to reduce computational overload.

^{1}H imaging is not significantly affected (< 5% change in regional SNR; Supporting Information Figure S8) by the presence of the ^{19}F coils. The anterior part of the Rx and Tx coils can be removed without moving the animal, whereas the posterior elements are unplugged and detuned during ^{1}H MRI. Thus, ^{19}F MRI can be performed as an add-on experiment, for example, to an MR-guided interventional procedure, and commercially available ^{1}H coil arrays can be used for ^{1}H imaging. A double-resonant coil was not preferred, as the combination of different resonance frequencies leads to a suboptimal performance.

The ^{19}F MRI system can be upscaled or downscaled for human measurements. The size of the Rx elements could be reduced for humans to increase the receive sensitivity. Similarly, the Tx coil efficiency can be increased by placing the coil elements closer to the patient. This concept was tested for decreasing the diameter of the Tx coil holder for the small pig model from 420 mm to 300 mm, and the Tx efficiency was increased by 40.2% around the center of the heart. The size of the coil was adapted by using adjustable coil holders such as in Lopez Rios et al.[58] This approach is especially suitable for the proposed Tx coil system, as each coil element is electrically and mechanically separated.

FDTD simulations with random deviations from the ideal CP mode showed that the Tx array is robust against phase and power deviations at the input ports. Although the Tx efficiency of quadrature birdcage coils is higher than that of the Tx array, the modular, scalable Tx array has several advantages: It is simple to build by 3D printing; it does not need electrical or mechanical connection between the elements; coil elements can be tuned independently and individually; and it can potentially be used with parallel Tx for RF shimming and local SAR management.[47,50,59] A birdcage coil can also be designed in multiple segments that can be attached together with robust galvanic connections between the pieces (eg, two half cylinders), yet

this would require other means of production equipment. However, we think a modular birdcage structure can also be constructed using rapid prototyping facilities such as printed circuit board etching and 3D printing, and being able to be replaced without moving the subject inside would be very useful; however, this is beyond scope of this study. Unlike birdcage coils, this coil can also be adapted to higher fields after retuning, without further modifications, as shown in Figure 5.

In both simulations and MRI experiments, the five-channel Tx array could provide sufficient Tx homogeneity within the heart and with the advantage of increased maximum B_1^+. This is especially useful for nuclei such as ^{19}F, for which only a limited peak RF power was available on the clinical MRI system we used (ie, 3.2 kW). If other organs such as the spleen are studied, the arrangement with reduced Tx channel needs to be further investigated.

The proposed coil array opens design options for densely packed multichannel transmit ^{19}F RF coil arrays, even at higher magnetic field strengths. Future solutions will involve designs that use different building blocks for signal transmission and reception, to balance the constraints dictated by sensitivity, depth penetration, transmission field uniformity, SNR, and SAR.[60] In this context, a recent report suggested the combination of dipole antenna and loop elements.[61] At 3 T, CP mode with fixed amplitude an phase distributions resulted in satisfactory β_1^+ homogeneity values with a maximum deviation of 17%, even for the five-channel Tx array arrangement. Our ^{19}F phantom studies with PFOB showed a steady ^{19}F signal over a series of independent measurements with a signal variability of 3%. A closer examination revealed a detection limit of 3.9 mmol (or 23×10^{20} PFOB molecules) for the proposed setup, accounting only for the CF_2Br spins.

In all measurements, a narrow-band RF pulse was used, which excited only the central resonance and ignored the other peaks in the spectrum. For complex ^{19}F molecular structures, optimized sequences that can excite the whole spectrum using larger RF bandwidths and prevent chemical shift artifacts at the same time are required to increase SNR. One possible approach could be to perform sine-bell acquisition-weighted CSI with selective refocusing pulses.[62]

Similar to the scalable Tx array idea, the proposed Rx array can also be designed in a scalable form to increase SNR from the target volume such as demonstrated in Lopez Rios et al.[58] Although the anterior part of the current Rx array has a semiflexible design and is placed directly on the abdomen, maximizing the filling factor, the size and geometric extent of the Rx array configuration can be modified to bring all of the elements closer to the heart region, even for smaller animals. This can be accomplished by designing all of the array elements as flexible modular coils,[42,63] or by keeping the four loop coils as the core structure and using the remaining two SLR elements as separate portable elements that can be placed closer to the heart in smaller animals. We designed the size of the proposed Rx array elements by considering the geometric extent of the heart from the anterior surface. This distance is smaller in smaller animals. A more straightforward approach would be to construct a downscaled version of the existing anterior part of the Rx array for smaller animals.

5 | CONCLUSIONS

The proposed modular eight-channel ^{19}F Tx and the eight-channel semiflexible Rx RF coil array is an important step to realize ^{19}F-MRI experiments in the heart, to assess the biodistribution and bioavailability of fluorinated drugs. The modular design allows us to adapt the coil array to pigs of various sizes, improving the Tx coil performance. The ^{19}F coil can be combined with existing ^{1}H coil equipment, which is advantageous in complex studies involving MR-guided interventions and functional imaging.

ACKNOWLEDGMENT

The authors thank Prof. Jim Wild and Dr. Madhwesha Rama Rao of the University of Sheffield for sharing their experiences in ^{19}F coil design. They also thank Dr. Muhammed Yildirim of University of Cologne for the fruitful discussions on ^{19}F substances and phantom design. Open Access funding enabled and organized by Projekt DEAL. This study was part of SFB1425, funded by the Deutsche Forschungsgemeinschaft (DFG, German Research Foundation) - Project #422681845.

FUNDING INFORMATION

German Research Foundation (BO 3025/17-1, MA 7059/3-1 and SFB1425 #422681845).

ORCID

Ali Caglar Özen https://orcid.org/0000-0003-3536-0826
Johannes Fischer https://orcid.org/0000-0003-1499-6163
Serhat Ilbey https://orcid.org/0000-0002-3574-4320
Simon Reiss https://orcid.org/0000-0003-2449-1679
Michael Bock https://orcid.org/0000-0001-9720-3506

REFERENCES

1. Nahrendorf M, Pittet MJ, Swirski FK. Monocytes: protagonists of infarct inflammation and repair after myocardial infarction. *Circulation*. 2010;121:2437-2445.
2. Nahrendorf M, Swirski FK. Monocyte and macrophage heterogeneity in the heart. *Circ Res*. 2013;112:1624-1633.

3. Temme S, Jacoby C, Ding Z, et al. Technical advance: monitoring the trafficking of neutrophil granulocytes and monocytes during the course of tissue inflammation by noninvasive 19F MRI. *J Leukoc Biol*. 2014;95:689-697.
4. Bönner F, Merx MW, Klingel K, et al. Monocyte imaging after myocardial infarction with 19F MRI at 3 T: a pilot study in explanted porcine hearts. *Eur Heart J Cardiovasc Imaging*. 2015;16:612-620.
5. Amiri H, Srinivas M, Veltien A, van Uden MJ, de Vries IJM, Heerschap A. Cell tracking using (19)F magnetic resonance imaging: technical aspects and challenges towards clinical applications. *Eur Radiol*. 2015;25:726-735.
6. Bönner F, Gastl M, Nienhaus F, et al. Regional analysis of inflammation and contractile function in reperfused acute myocardial infarction by in vivo 19F cardiovascular magnetic resonance in pigs. *Basic Res Cardiol*. 2022;117:21.
7. Choi CH, Hong SM, Felder J, Shah NJ. The state-of-the-art and emerging design approaches of double-tuned RF coils for X-nuclei, brain MR imaging and spectroscopy: a review. *Magn Reson Imaging*. 2020;72:103-116.
8. Schnall M, Harihara Subramanian V, Leigh J, Chance B. A new double-tuned probed for concurrent 1H and 31P NMR. *J Magn Reson*. 1985;65:122-129.
9. Rath AR. Design and performance of a double-tuned bird-cage coil. *J Magn Reson*. 1990;86:488-495.
10. Lim H, Thind K, Martinez-Santiesteban FM, Scholl TJ. Construction and evaluation of a switch-tuned 13 C - 1 H birdcage radiofrequency coil for imaging the metabolism of hyperpolarized 13 C-enriched compounds. *J Magn Reson Imaging*. 2014;40:1082-1090.
11. Pratt R, Giaquinto R, Ireland C, et al. A novel switched frequency 3 he/ 1 H high-pass birdcage coil for imaging at 1.5 tesla. *Concepts Magn Reson Part B Magn Reson Eng*. 2015;45:174-182.
12. Amari S, Müfit Ulug A, Bornemann J, PCM VZ, Barker PB. Multiple tuning of birdcage resonators. *Magn Reson Med*. 1997;37:243-251.
13. Matson GB, Vermathen P, Hill TC. A practical double-tuned1H/31P quadrature birdcage headcoil optimized for31P operation. *Magn Reson Med*. 1999;42:173-182.
14. Murphyboesch J, Srinivasan R, Carvajal L, Brown TR. Two configurations of the four-ring birdcage coil for 1H imaging and 1H-decoupled 31P spectroscopy of the human head. *J Magn Reson Ser B*. 1994;103:103-114.
15. Joseph PM, Lu D. A technique for double resonant operation of birdcage imaging coils. *IEEE Trans Med Imaging*. 1989;8:286-294.
16. Lu D, Joseph PM. A technique of double-resonant operation of19F and1H quadrature birdcage coils. *Magn Reson Med*. 1991;19:180-185.
17. Muftuler LT, Gulsen G, Sezen KD, Nalcioglu O. Automatic tuned MRI RF coil for multinuclear imaging of small animals at 3T. *J Magn Reson*. 2002;155:39-44.
18. Hu L, Hockett FD, Chen J, et al. A generalized strategy for designing 19F/1H dual-frequency MRI coil for small animal imaging at 4.7 tesla. *J Magn Reson Imaging*. 2011;34:245-252.
19. Choi C-H, Hong S-M, Ha Y, Shah NJ. Design and construction of a novel 1 H/ 19 F double-tuned coil system using PIN-diode switches at 9.4 T. *J Magn Reson*. 2017;279:11-15.
20. Asfour A. A three-coil RF probe-head at 2.35 T: potential applications to the 23Na and to the hyperpolarized 129Xe MRI in small animals. In: *Proceedings of the Annual International Conference of the IEEE Engineering in Medicine and Biology*, Buenos Aires, Argentina, 2010. pp. 5693–5699. IEEE.
21. Fitzsimmons JR, Beck BL, Ralph BH. Double resonant quadrature birdcage. *Magn Reson Med*. 1993;30:107-114.
22. Hudson AMJ, Köckenberger W, Bowtell RW. Dual resonant birdcage coils for1H detected13C microscopic imaging at 11.7 T. *Magma Magn Reson Mater Phys Biol Med*. 2000;10:61-68.
23. Brand RC, Webb AG, Beenakker J-WM. Design and performance of a transformer-coupled double resonant quadrature birdcage coil for localized proton and phosphorus spectroscopy in the human calf muscle at 7 T. *Concepts Magn Reson Part A*. 2013;42:155-164.
24. Meyerspeer M, Roig ES, Gruetter R, Magill AW. An improved trap design for decoupling multinuclear RF coils. *Magn Reson Med*. 2014;72:584-590.
25. Alecci M, Romanzetti S, Kaffanke J, Celik A, Wegener HP, Shah NJ. Practical design of a 4 tesla double-tuned RF surface coil for interleaved 1H and 23Na MRI of rat brain. *J Magn Reson*. 2006;181:203-211.
26. Bottomley PA, Hardy CJ, Roemer PB, Mueller OM. Proton-decoupled, overhauser-enhanced, spatially localized carbon-13 spectroscopy in humans. *Magn Reson Med*. 1989;12:348-363.
27. Alfonsetti M, Sotgiu A, Alecci M. Design and testing of a 1.5 tesla double-tuned (1H/31P) RF surface coil with intrinsic geometric isolation. *Measurement*. 2010;43:1266-1276.
28. Adriany G, Gruetter R. A half-volume coil for efficient proton decoupling in humans at 4 tesla. *J Magn Reson*. 1997;125:178-184.
29. Yan X, Xue R, Zhang X. A monopole/loop dual-tuned RF coil for ultrahigh field MRI. *Quant Imaging Med Surg*. 2014;4:225-231.
30. Rutledge O, Kwak T, Cao P, Zhang X. Design and test of a double-nuclear RF coil for 1 H MRI and 13 C MRSI at 7 T. *J Magn Reson*. 2016;267:15-21.
31. Ji Y, Waiczies H, Winter L, et al. Eight-channel transceiver RF coil array tailored for 1H/19F MR of the human knee and fluorinated drugs at 7.0 T. *NMR Biomed*. 2015;28:726-737.
32. Klomp D, Van Laarhoven H, Scheenen T, Kamm Y, Heerschap A. Quantitative 19F MR spectroscopy at 3 T to detect heterogeneous capecitabine metabolism in human liver. *NMR Biomed*. 2007;20:485-492.
33. Maunder A, Rao M, Robb F, Wild JM. Comparison of MEMS switches and PIN diodes for switched dual tuned RF coils. *Magn Reson Med*. 2018;80:1746-1753.
34. Rothe M, Jahn A, Weiss K, et al. In vivo 19F MR inflammation imaging after myocardial infarction in a large animal model at 3 T. *Magn Reson Mater Phys Biol Med*. 2019;32:5-13.
35. Choi C-H, Ha Y, Veeraiah P, Felder J, Möllenhoff K, Shah NJ. Design and implementation of a simple multinuclear MRI system for ultra high-field imaging of animals. *J Magn Reson*. 2016;273:28-32.
36. Gareis D, Neuberger T, Behr VC, Jakob PM, Faber C, Griswold MA. Transmit-receive coil-arrays at 17.6T, configurations for 1H, 23Na, and 31P MRI. *Concepts Magn Reson Part B Magn Reson Eng*. 2006;29B:20-27.
37. Fedorov A, Beichel R, Kalpathy-Cramer J, et al. 3D slicer as an image computing platform for the quantitative imaging network. *Magn Reson Imaging*. 2012;30:1323-1341.

38. Zabel HJ, Bader R, Gehrig J, Lorenz WJ. High-quality MR imaging with flexible transmission line resonators. *Radiology*. 1987;165:857-859.
39. Stensgaard A. Optimized design of the shielded-loop resonator. *J Magn Reson Ser A*. 1996;122:120-125.
40. Harpen MD. The theory of shielded loop resonators. *Magn Reson Med*. 1994;32:785-788.
41. Frass-Kriegl R, Laistler E, Hosseinnezhadian S, et al. Multi-turn multi-gap transmission line resonators—concept, design and first implementation at 4.7 T and 7 T. *J Magn Reson*. 2016;273:65-72.
42. Sreereddy M, Bock M, Özen AC. Optimization and analysis of shielded loop resonators towards modular coil arrays. In: Proceedings of the 30th Annual Meeting of ISMRM, United Kingdom, 2022. p. 47.
43. Hasgall PA, Di Gennaro F, Baumgartner C, et al. IT'IS database for thermal and electromagnetic parameters of biological tissues. 2012. doi: 10.13099/VIP21000-04-0.
44. Bomsdorf H, Helzel T, Kunz D, Röschmann P, Tschendel O, Wieland J. Spectroscopy and imaging with a 4 tesla whole-body mr system. *NMR Biomed*. 1988;1:151-158.
45. Barfuss H, Fischer H, Hentschel D, Ladebeck R, Vetter J. Whole-body MR imaging and spectroscopy with a 4-T system. *Radiology*. 1988;169:811-816.
46. Ibrahim TS, Lee R, Baertlein BA, Abduljalil AM, Zhu H, Robitaille P-ML. Effect of RF coil excitation on field inhomogeneity at ultra high fields: a field optimized TEM resonator. *Magn Reson Imaging*. 2001;19:1339-1347.
47. Zhu Y. Parallel excitation with an array of transmit coils. *Magn Reson Med*. 2004;51:775-784.
48. Adriany G, Van de Moortele P-F, Wiesinger F, et al. Transmit and receive transmission line arrays for 7 tesla parallel imaging. *Magn Reson Med*. 2005;53:434-445.
49. Wald LL, Wiggins GC, Potthast A, Wiggins CJ, Triantafyllou C. Design considerations and coil comparisons for 7 T brain imaging. *Appl Magn Reson*. 2005;29:19.
50. Katscher U, Börnert P. Parallel RF transmission in MRI. *NMR Biomed*. 2006;19:393-400.
51. Jones DR, Schonlau M, Welch WJ. Efficient global optimization of expensive black-box functions. *J Glob Optim*. 1998;13:455-492.
52. Balezeau F, Eliat P-A, Cayamo AB, Saint-Jalmes H. Mapping of low flip angles in magnetic resonance. *Phys Med Biol*. 2011;56:6635-6647.
53. Shukla HP, Mason RP, Woessner DE, Antich PP. A comparison of three commercial perfluorocarbon emulsions as high-field 19F NMR probes of oxygen tension and temperature. *J Magn Reson Ser B*. 1995;106:131-141.
54. Henkelman RM. Measurement of signal intensities in the presence of noise in MR images. *Med Phys*. 1985;12:232-233.
55. World Health Statistics. 2021. Accessed October 2, 2022. https://www.who.int/data/stories/world-health-statistics-2021-a-visual-summary.
56. van der Laan AM, ter Horst EN, Delewi R, et al. Monocyte subset accumulation in the human heart following acute myocardial infarction and the role of the spleen as monocyte reservoir. *Eur Heart J*. 2014;35:376-385.
57. Carluccio G, Akgun C, Vaughan JT, Collins C. Temperature-based MRI safety simulations with a limited number of tissues. *Magn Reson Med*. 2021;86:543-550.
58. Lopez Rios N, Foias A, Lodygensky G, Dehaes M, Cohen-Adad J. Size-adaptable 13-channel receive array for brain MRI in human neonates at 3 T. *NMR Biomed*. 2018;31:e3944.
59. Sadeghi-Tarakameh A, Radder J, Lagore RL, et al. Safety assessment of custom-built multi-channel RF coils: EM modeling uncertainties. *Proceedings of the 30th Annual Meeting of ISMRM, London, United Kingdom*. International Society of Magnetic Resonance in Medicine; 2022:583.
60. Lattanzi R, Sodickson DK. Ideal current patterns yielding optimal signal-to-noise ratio and specific absorption rate in magnetic resonance imaging: computational methods and physical insights. *Magn Reson Med*. 2012;68:286-304.
61. Ertürk MA, Raaijmakers AJE, Adriany G, Uğurbil K, Metzger GJ. A 16-channel combined loop-dipole transceiver array for 7 Tesla body MRI. *Magn Reson Med*. 2017;77:884-894.
62. Jacoby C, Temme S, Mayenfels F, et al. Probing different perfluorocarbons for in vivo inflammation imaging by 19 F MRI: image reconstruction, biological half-lives and sensitivity. *NMR Biomed*. 2014;27:261-271.
63. Özen AC, Taege Y, Lottner T, Ilbey S, Ataman Ç, Bock M. *Light coils: MRI with modular RF coils using optical power and data transmission*. In: Proceedings of the 30th Annual Meeting of ISMRM, United Kingdom, 2022. p. 186.

SUPPORTING INFORMATION

Additional supporting information may be found in the online version of the article at the publisher's website.

FIGURE S1: Schematic diagram for interfacing the transmit (Tx) array to the MRI system. A coil plug (Tx plug) was used to deliver the RF power from a broadband RF power amplifier (RFPA), as well as the DC bias voltage for active detuning of the individual Tx coil elements, as shown in the detuning circuit for the first element. The detuning logic is predefined in the coil files, which is controlled through the RF excitation and signal acquisition entries in the pulse sequence. To avoid excessive cabling, the DC signals were coupled with the RF paths, leading to the individual Tx coil elements at the power splitter

FIGURE S2: Schematic diagram for interfacing the receive (Rx) coils to the MRI system. A coil plug (Rx plug) was used to deliver the amplified MR signal to the receiver unit of the MRI system, as well as the DC bias voltage for active detuning of the individual Rx coil elements. Detuning circuits for loop and shielded loop resonator (SLR) elements are shown for the first elements. An additional cross-diode is used at the preamplifier inputs (not shown) after the DC-blocking capacitor, C_{dc}, for passive protection. Preamplifiers were biased through the "MR signal" path, which is a coaxial cable with a DC signal coupled, which is activated during the receive cycle. The detuning logic is predefined in the coil files, which is controlled via the RF excitation and signal acquisition entries in the pulse sequence. To avoid excessive cabling, the DC signals for

active detuning were also coupled with the RF paths on the coil side

FIGURE S3: Comparison of the next-nearest-neighbor distances in the four-loop array 2×2 configurations. A, B, The proposed approach in (A) results in a distance of 5.5 cm between L11 and L22, whereas the arrangement in (B) a distance of 1.4 cm. Additional decoupling of 4.3 dB between L11 and L22 is gained by choosing (A) over (B)

FIGURE S4: A schematic diagram of the battery-supplied detuning used for the unplugged 19F coils that are left inside the magnet bore during ^{1}H measurements. The battery output is simply connected to the coaxial cable of the 19F coil elements, thereby activating the detuning PIN diode to minimize coupling with the ^{1}H coils

FIGURE S5: Line profile results of the simulations for various pig model and coil pairs in the ideal input matching case normalized to 1-kW input power. Magnitude of the B_1^+ field was plot along the lines in L1 (head–foot), L2 (anterior–posterior), and L3 (right–left) directions for each combination

FIGURE S6: Effect of the phase and amplitude mismatches on the B_1^+ homogeneity. Thirty-two random amplitude and phase values within 20% of the ideal values were used to calculate field distributions and maximum deviation from the mean along the lines in L1 (head–foot), L2 (anterior–posterior), and L3 (right–left) directions

FIGURE S7: PFOB was mixed with FC-84 (perfluoroheptane) to test sensitivity of the coils by exciting only the CF2Br peak of perfluoroctylbromide (PFOB) using a narrow-band (3 kHz) Gaussian RF pulse. The image SNR for a 2-mm isotropic FLASH sequence (32 averages) was < 10 for the 5-ml tubes with 10% and 25% solutions

FIGURE S8: Comparison of ^{1}H gradient-echo (GRE) images with and without the remaining 19F elements, which were actively detuned. No significant artifacts or sensitivity change was observed with structural similarity index (SSIM) of 0.9913 and normalized mean square error (NMSE) of 0.55%

How to cite this article: Özen AC, Spreter F, Schimpf W, et al. Scalable and modular 8-channel transmit and 8-channel flexible receive coil array for ^{19}F MRI of large animals. *Magn Reson Med*. 2023;89:1237-1250. doi: 10.1002/mrm.29490